Doped Materials

International Edition: DOI: 10.1002/anie.201503410
German Edition: DOI: 10.1002/ange.201503410

Atomic-Layer-Confined Doping for Atomic-Level Insights into Visible-Light Water Splitting**

Fengcai Lei, Lei Zhang, Yongfu Sun, Liang Liang, Katong Liu, Jiaqi Xu, Qun Zhang,* Bicai Pan, Yi Luo, and Yi Xie**

Abstract: *A model of doping confined in atomic layers is proposed for atomic-level insights into the effect of doping on photocatalysis. Co doping confined in three atomic layers of In_2S_3 was implemented with a lamellar hybrid intermediate strategy. Density functional calculations reveal that the introduction of Co ions brings about several new energy levels and increased density of states at the conduction band minimum, leading to sharply increased visible-light absorption and three times higher carrier concentration. Ultrafast transient absorption spectroscopy reveals that the electron transfer time of about 1.6 ps from the valence band to newly formed localized states is due to Co doping. The 25-fold increase in average recovery lifetime is believed to be responsible for the increased of electron–hole separation. The synthesized Co-doped In_2S_3 (three atomic layers) yield a photocurrent of 1.17 mA cm^{-2} at 1.5 V vs. RHE, nearly 10 and 17 times higher than that of the perfect In_2S_3 (three atomic layers) and the bulk counterpart, respectively.*

The increasingly serious energy crisis and the environmental contamination caused by burning fossil fuels have triggered an aggressive search for renewable and environmentally benign alternative energy recourses.[1–4] In this respect, solar fuel production of H_2 from H_2O and of hydrocarbons from CO_2 through direct photoelectrochemical reactions has been recognized as a promising approach to pursue renewable energy sources.[1,5] Note that the only oxidation reaction that can balance these fuel-forming reduction reactions is the production of O_2, in which many exceptional semiconductors, such as the H:TiO_2 nanowires, nanoporous $BiVO_4$ with a FeOOH and NiOOH dual-layer, NiFe LDH/Ni foam, and W gradient-doped $BiVO_4$ film, have been widely researched as photoanodes for oxygen production in the past few years.[6–9] The photoelectrochemical water oxidation usually contains three successive processes: 1) photoabsorption to generate electron–hole pairs; 2) separation and transport of photogenerated electron–hole pairs; and 3) oxidization of water into O_2 by photogenerated holes.[4,10,11] The first two processes are strongly dependent on the atomic and/or electronic structure of the photocatalysts, and especially the kinetically sluggish electron–hole separation/transport is one of the main factors that limit the photoelectrochemical water splitting efficiency. To address this limitation and improve the solar conversion efficiency, enormous efforts have been focused on modifying the electronic structure of semiconductor photocatalysts by elemental doping. For example, TiO_2 doped with transition-metal ions such as iron, nickel, cobalt, and chromium could extend its light absorption from UV to the visible region by introducing additional energy levels within the band gap of TiO_2.[12,13] Another example has shown that the doped transition-metal Co ions could also serve as trap sites to capture the photogenerated electrons or holes from ZnO and hence reduce the electron–hole recombination, thereby achieving improved photocatalytic efficiency.[14] Notably, almost all of the transition-metal dopants are present on the interior of photocatalysts, rather than on the surface, which would cause contradictory results. For instance, there have also been other experimental results to verify that the transition-metal dopants in TiO_2 could act as the recombination centers, resulting in limited improvement in photocatalytic activity (or even lower than pure TiO_2).[15,16] The ongoing debate over the role of elemental doping in photocatalysis has hampered further progress in realizing higher photoconversion efficiency. Such controversy is probably due to the large discrepancies between idealized models and real catalysts with abundant microstructures such as surface, interface, grain boundary, and defect, which would adversely affect or cover the effect of elemental doping on photocatalytic activity. To gain in-depth atomic-level understanding on the relationship between elemental doping and solar water splitting, it would be rather imperative to simplify the catalyst model and bridge it with the real doped catalyst.

Herein, conceptually new doping confined in atomic layers is first put forward as an ideal material model for disclosing atomic-level insights into the role of elemental doping in photocatalysis. Taking the non-toxic and mid-band-gap semiconductor of cubic-In_2S_3 (crystal structure in the

[*] F. Lei,[+] L. Zhang,[+] Prof. Y. Sun, L. Liang, K. Liu, J. Xu, Prof. Q. Zhang, Prof. B. Pan, Prof. Y. Luo, Prof. Y. Xie
Hefei National Laboratory for Physical Sciences at Microscale, Collaborative Innovation Center of Chemistry for Energy Materials, Synergetic Innovation Center of Quantum Information and Quantum Physics, University of Science & Technology of China
Hefei, Anhui 230026 (P.R. China)
E-mail: yfsun@ustc.edu.cn
qunzh@ustc.edu.cn
yxie@ustc.edu.cn

[+] These authors contributed equally to this work.

[**] This work was financially supported by the National Natural Science Foundation of China (21331005, 21422107, 21201157, 91422303, 11321503, 21173205, 91127042), the Chinese Academy of Sciences (XDB01020000), the Program for New Century Excellent Talents in University (NCET-13-0546), the Youth Innovation Promotion Association of CAS (CX2340000100), and the Fundamental Research Funds for the Central Universities No. WK2340000063. Supercomputing center of USTC is acknowledged for computational support.

Supporting information for this article is available on the WWW under http://dx.doi.org/10.1002/anie.201503410.

Supporting Information, Figure S1 A)[17] as an example, we construct perfect In_2S_3 as three atomic layers (3ALs) and Co-doped In_2S_3 3ALs and implement density-functional-theory (DFT) calculations to study the effect of Co doping on the electronic structure at atomic level. Evidently, as revealed by the calculated density of states (DOS) shown in Figure 1 A and the crystal structure in the Supporting Information, Figure S1 B, the presence of Co dopant endows the In_2S_3 3AL slab with obviously increased DOS at conduction band minimum (CBM) with respect to the perfect In_2S_3 3AL slab. More importantly, the introduction of Co ions gives rise to several new energy levels in the Co-doped In_2S_3 3AL slab, which could be ascribed to the splitting of Co 3d states.[18] In this case, the photogenerated electrons can be easily excited via the d→d internal transition of Co ions in tetrahedral coordination under solar light irradiation, opening the possibility to achieve higher photoconversion efficiency.[12,18,19] Moreover, from the spatial distribution of the charge density at CBM of the Co-doped In_2S_3 3AL slab (Figure 1 B), it can clearly be seen that the vast majority of charge density originates from the Co and S atoms, suggesting that most of the Co dopants confined in atomic layers could be directly involved in the photocatalytic reaction and hence cause significant improvement in photocatalytic activity. Furthermore, Figure 1 C–F reveals that the perfect In_2S_3 3AL slab also exhibits an obviously increased DOS at the conduction band edge as compared with its bulk counterpart, which is further demonstrated by the corresponding distribution of charge density. As such, our DFT results suggest that the overwhelming majority of Co dopants distributed on the In_2S_3 3ALs surface facilitates easier electron excitation and allows for higher carrier density as well as efficient carrier transport along the two-dimensional (2D) conducting channels.[20–22]

To uncover the question of how doping matters in photocatalysis, it is indispensable to synthesize In_2S_3 3ALs with/without Co doping in the first place. However, for the cubic-In_2S_3 with a nonlayered structure (Supporting Information, Figure S1 A), the lack of intrinsic driving force for 2D anisotropic growth renders the fabrication of In_2S_3 atomic layers a grand challenge, let alone the synthesis of doped In_2S_3 atomic layers. Herein, we develop a scalable lamellar inorganic–organic hybrid intermediate strategy for fabricating the atomically thin, 2D semiconductor sheets doped with transition-metal ions (Figure 2 A). Taking Co-doped In_2S_3 as a prototype, a lamellar In/Co-oleate hybrid complex is initially synthesized by electrostatic interaction between In^{3+}, Co^{2+}, and oleate ions, in which the ordered mesostructure is confirmed by their corresponding series of small-angle XRD peaks with a layer spacing of 4.41 nm (Supporting Information, Figure S2), which is roughly twice the fully stretched oleate-ion length, suggesting a head-to-head (or tail-to-tail) bilayer arrangement of oleate ions in this mesostructure.[23] With the addition of sulfur powder followed by hydrothermal treatment, In_2S_3 doped with Co ions grows along the lamellar In/Co-oleate hybrid mesostructure, while the continuously proceeded reaction simultaneously facilitates the self-exfoliation of the lamellar mesostructure into

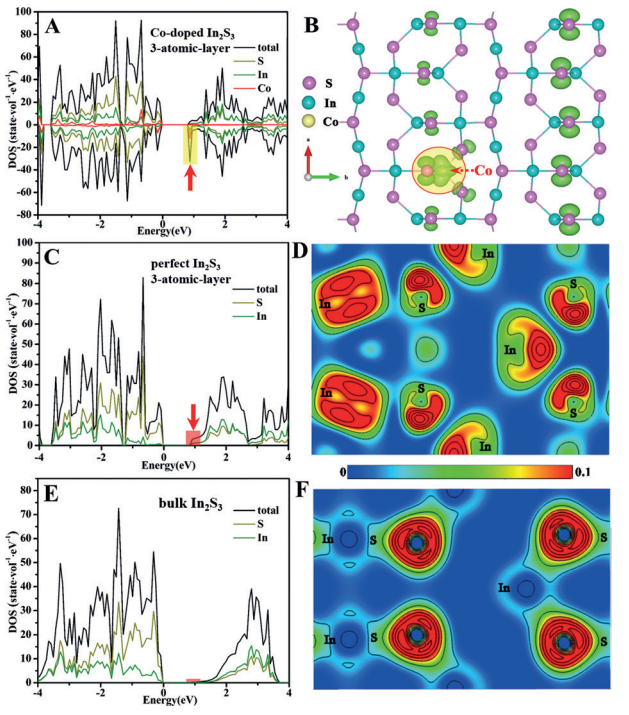

Figure 1. A), C), E) DFT calculations: calculated density of states of A) Co-doped In_2S_3 three atomic layer slab, C) perfect In_2S_3 three atomic layer slab, and E) bulk In_2S_3. B), D), F) The distribution of charge density of the conduction band edge of B) Co-doped In_2S_3 three atomic layer slab D) perfect In_2S_3 three atomic layer slab, and F) bulk In_2S_3. Black lines in (D) and (F) represent the contour lines of the charge density.

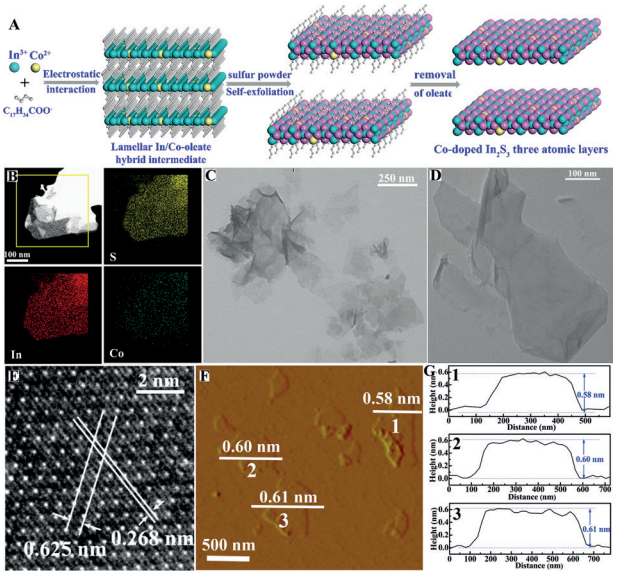

Figure 2. A) Representation of the formation of Co-doped In_2S_3 three atomic layers; B)–G) Characterizations for the Co-doped In_2S_3 three atomic layers: B) HAADF-STEM image and corresponding EDS mapping images of an individual Co-doped In_2S_3 three atomic layer, indicating the homogeneous distribution of indium, sulfur, and cobalt; C), D) TEM images; E) HRTEM image; F) AFM image, and G) the corresponding height profiles; the numbers from 1 to 3 in (G) correspond to the numbers from 1 to 3 in (F).

freestanding Co-doped In_2S_3 atomic layers. Owing to the very weak electrostatic interaction between the oleate ions and Co-doped In_2S_3 atomic layers, the surface oleate ions can be removed through washing with cyclohexane and absolute ethanol for many times, thereby leading to the formation of clean Co-doped In_2S_3 atomic layers as further indicated by the FTIR spectrum (Supporting Information, Figure S3).

It should be noted that the XRD measurement is carried out on the collected powder sample aggregated by the as-prepared Co-doped In_2S_3 atomic layers, which is due to the current infeasibility to perform XRD characterization on individual ultrathin sheet. The corresponding XRD pattern (Supporting Information, Figure S4) can be readily indexed to the cubic-In_2S_3 (JCPDS No. 65-0459), while the corresponding XPS spectra (Supporting Information, Figure S5) demonstrate the presence of In^{3+}, S^{2-}, and Co^{2+}. Additionally, the HAADF-STEM image and the corresponding element mapping analyses (Figure 2B) reveal the homogeneous distribution of In, S, and Co in the whole selection area of an ultrathin nanosheet. These results suggest that the homogeneous Co doping at the atomic level does not change the cubic structure of In_2S_3. ICP result indicates that the concentration of Co is about 3%. TEM image (Figure 2C,D) shows the nearly transparent sheet-like morphology, while the corresponding high-resolution TEM image (Figure 2E) illustrates its preferential growth orientation along the [0 1 −1] projection. Also, the AFM image and the corresponding height profiles (Figure 2F,G) identify that the overwhelming majority of the Co-doped In_2S_3 sheets possesses an average height of about 0.59 nm, which is consistent with the three atomic thickness of In_2S_3 3AL slab along the [0 1 −1] direction. Therefore, all the aforementioned results unambiguously demonstrate the formation of clean Co-doped In_2S_3 ultrathin sheets with three atomic thickness.

To disclose the function of cobalt substitution in In_2S_3 3ALs in the solar water splitting, it is essential to evaluate the photoelectrochemical water oxidation properties of Co-doped In_2S_3 3ALs, perfect In_2S_3 3ALs (Supporting Information, Figure S6–S7), and bulk counterpart (Supporting Information, Figure S8). The photoelectrodes are prepared by spin coating the corresponding ethanol dispersions on indium tin oxide (ITO)-coated glass. As displayed in Figure 3A, all the three photoelectrodes possess negligible dark currents at the applied potentials between 1.0 and 1.5 V (vs. RHE). Contrastingly, under visible-light irradiation from a 300-W Xe lamp with a standard AM 1.5G filter, the perfect In_2S_3 3ALs-based photoelectrode exhibits obviously increased oxidation current densities with respect to the bulk In_2S_3-based photoelectrode, indicating higher photoactivity of the ultrathin In_2S_3 atomic layers. Most strikingly, the Co-doped In_2S_3 3ALs-based photoelectrode shows superior oxidation current densities to the perfect In_2S_3 3ALs-based photoelectrode over the entirely applied potentials. For example, the Co-doped In_2S_3 3ALs-based photoelectrode attains a photocurrent density of 1.17 mA cm^{-2} at the applied potential of 1.5 V (vs. RHE), nearly 10 and 17 times higher than that of the perfect In_2S_3 3ALs and the bulk In_2S_3-based photoelectrodes, respectively. These results strongly demonstrate that the introduction of Co ions brings fantastic advantages of

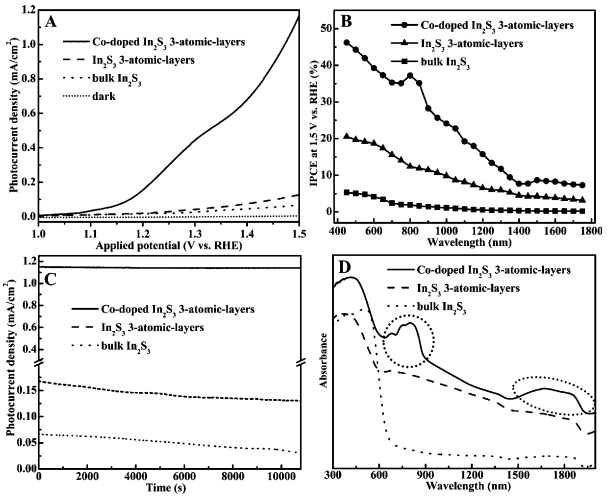

Figure 3. Photoelectrochemical properties for Co-doped In_2S_3 three atomic layers, pure In_2S_3 three atomic layers, and the bulk counterpart. A) Photocurrent density vs. applied potential curves under 300 W Xe lamp irradiation ($\lambda > 420$ nm); B) IPCE at 1.5 V vs. RHE; C) *I–t* curve at 1.5 V vs. RHE under 300 W Xe lamp irradiation ($\lambda > 420$ nm); D) UV/Vis diffuse reflectance spectra; the dotted line rings denote the sharply increased photoabsorption.

significantly promoting the visible-light water splitting. Note that incident photon-to-current conversion efficiency (IPCE), being independent of the light sources and filters utilized in the measurements,[6] is thought of as a more direct means for evaluating the photoconversion efficiency. As shown in Figure 3B, the perfect In_2S_3 3ALs-based photoelectrode achieves higher IPCE than the bulk In_2S_3-based photoelectrode in the wavelength range of 450–1750 nm. Markedly, the Co-doped In_2S_3 3ALs-based photoelectrode performs further improved IPCE, reaching a value up to 46% at 450 nm, which is over 2 and 9 times higher than that of the perfect In_2S_3 3ALs and bulk In_2S_3-based photoelectrodes, respectively. More importantly, the Co-doped In_2S_3 3ALs-based photoelectrode exhibits sharply increased IPCE in the two wavelength ranges of 750–900 and 1500–1750 nm, indicating their dramatically promoted visible-light conversion efficiency. Furthermore, photostability is generally regarded as one of the most important factors for evaluating the solar water splitting performance. Figure 3C clearly shows that the Co-doped In_2S_3 3ALs-based photoelectrode still retains almost the same photocurrent density as the initial value even after 10800 s irradiation, while the perfect In_2S_3 3ALs and bulk In_2S_3-based photoelectrodes exhibit obvious *I–t* fluctuations, clearly revealing the superior structural stability of the former. The evolved H_2 and O_2 contents were also measured by gas chromatography. As shown in the Supporting Information, Figure S9, the evolved rate of H_2 gas is roughly two times larger than that of O_2 gas, consisting with the principle of water splitting into H_2 and O_2. Also, both the experimental evolved rates of H_2 and O_2 gases are close to the corresponding theoretical values of H_2 and O_2 gases, indicating that there no obvious photocorrosion occurred on the Co-doped In_2S_3 3ALs-based photoelectrode. Taken together, the above results strongly verify that Co doping at the atomic level is

indeed highly beneficial for improving the visible-light conversion efficiency and also conferring the enhanced photostability.

The substantial improvement in visible-light water splitting could be primarily attributed to the Co doping confined in In_2S_3 3ALs, which helps to fully optimize the three elementary processes during photoelectrochemical water splitting. The In_2S_3 3ALs with ultralarge specific surface area can provide tremendous surface atoms to serve as the active sites for harvesting sunlight,[2,3,24] as verified by their significantly increased photoabsorption over the entire wavelengths ranging from 600 to 2000 nm (Figure 3D). Furthermore, the incorporation of Co ions into In_2S_3 3ALs further helps to improve their photoabsorption, especially in the visible-light region. It is worth noting that the increased light absorption before 650 nm for the Co-doped In_2S_3 3ALs as compared to that of the perfect In_2S_3 3ALs could be attributed to the formation of dopant energy levels of Co in the band gap of In_2S_3, in which the photogenerated electrons can be easily transferred from the valence band of In_2S_3 to the newly formed localized state of high-spin Co^{2+} ($3d^7$) in tetrahedral coordination.[12,19] Meanwhile, the sharply enhanced absorption in the region of 650–900 nm could be ascribed to the $^2E(G)$, $^4T_1(P)$, 2 $A_1(G)$→ground state 4 $A_2(F)$ transitions for high-spin Co^{2+} ($3d^7$) in tetrahedral coordination (d→d internal transitions), while the increased absorption in the region of 1500–1900 nm corresponds to the transition from $^4T_1(^4F)$→ground state $^4A_2(F)$, in which the fully occupied electrons in e levels can be easily excited to the unoccupied t_2 levels by absorption of visible light, thus resulting in a superior visible-light conversion efficiency (Figure 3B).[12,18,19,25] Furthermore, it would be very helpful to gain insights into the effect of Co doping on the electron dynamics involved. To this end, we employ ultrafast transient absorption (TA) spectroscopy to investigate the Co-doped In_2S_3 3ALs with reference to the In_2S_3 3ALs. In the TA measurements, a femtosecond UV pump/white-light continuum (WLC) probe Scheme is adopted (see the Supporting Information for details of the pump-probe experiments). The center wavelength of the pump pulses is chosen at 400 nm, which is proven suitable for effectively promoting electrons from the valence band to the conduction band of both In_2S_3 3ALs and Co-doped In_2S_3 3ALs (Figure 3D). Since the 450–670 nm WLC probe turns out to yield essentially the same TA kinetics for each sample, we show here a set of representative data taken at 510 nm (Figure 4A,B). Remarkably, the TA kinetics for the two samples differ significantly. As shown in Figure 4A, the In_2S_3 3ALs feature probe bleach signals immediately upon pump-laser excitation (that is, within the instrument response function time of about 100 fs in the vicinity of initial probe delay time zero). The subsequent probe bleach recovery is characterized by two time constants: $\tau_1 = 2.5 \pm 0.5$ ps and $\tau_2 = 27 \pm 4$ ps with a roughly 50:50 percentage for the two exponential components, and hence the average recovery lifetime in this case is estimated to be about 14 ps. In stark contrast, the Co-doped In_2S_3 3ALs exhibit photoinduced absorption (PA) signals as shown in Figure 4B, which feature an initial, circa 1.6 ps signal build-up followed by two exponential recovery processes (also in a roughly 50:50 percentage): $\tau_1 = 128 \pm 64$ ps and $\tau_2 = 555 \pm 203$ ps. Note that the average recovery lifetime in this case is estimated to be about 360 ps, which is roughly 25 times longer than that of the In_2S_3 3ALs. On the basis of the above representative observations on TA kinetics, useful information can be deduced concerning the electron dynamics involved. On the one hand, for the Co-doped In_2S_3 3ALs the PA signal build-up time of about 1.6 ps can be understood in terms of the photogenerated electron transfer from the valence band of In_2S_3 to the newly formed localized states owing to Co doping confined in In_2S_3 3ALs, which also provides experimental evidence for the aforementioned results of our DFT calculations (Figure 1A). On the other hand, the average recovery lifetime, no matter the TA signal recovery manifests itself in the form of probe bleach or of PA, can be regarded as a crude yet rational measure for evaluating the efficacy of photogenerated electron–hole separation involved in the investigated system. In this particular case study, the circa 25-fold increase in average recovery lifetime (that is, ca. 360 ps for Co-doped In_2S_3 3ALs vs. ca. 14 ps for In_2S_3 3ALs) should be strongly correlated with Co doping confined in In_2S_3 3ALs. From the electron dynamics perspective, it is safe to infer that such a dramatic lifetime increase in Co-doped In_2S_3 3ALs most likely accounts for the greatly improved photoconversion efficiency.

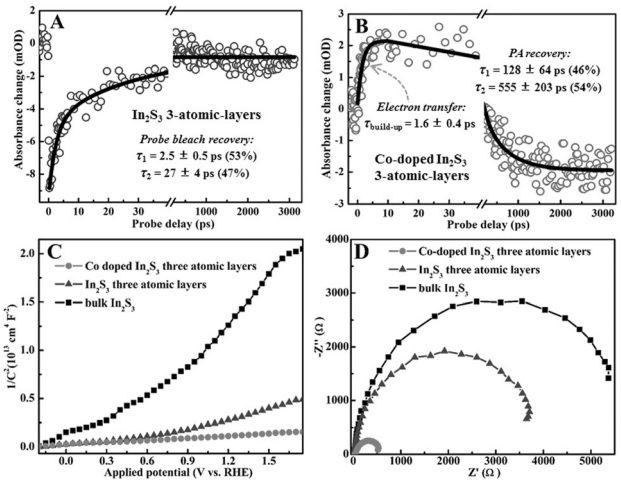

Figure 4. Ultrafast TA spectroscopy of A) In_2S_3 three atomic layers and B) Co-doped In_2S_3 three atomic layers. The TA kinetic traces shown here were recorded using a 400 nm pump and taken at a representative probing wavelength at 510 nm. C) Mott–Schottky plots and D) electrochemical impedance spectra at 1.5 V vs. RHE under 300-W Xe lamp irradiation ($\lambda > 420$ nm) for Co-doped In_2S_3 three atomic layers, pure In_2S_3 three atomic layers, and the bulk counterpart.

As a matter of fact, our DFT results shown in Figure 1C–F clearly reveal that the perfect In_2S_3 3ALs exhibit increased DOS at the CBM with respect to the bulk counterpart, while the introduction of Co ions further leads to a higher DOS near the CBM, in which the vast majority of charge density originates from the doped Co as well as S (Figure 1A,B). This is beneficial for realizing higher carrier concentration, which could be confirmed by their corresponding carrier density (N_D) calculated by the Mott–Schottky Equation. The N_D value for the Co-doped In_2S_3 3ALs is estimated to be 1.39 ×

10^{19} cm^{-3} (Figure 4C), which is roughly 3 and 13 times higher than that of the perfect In_2S_3 3ALs and bulk In_2S_3, respectively, which is fairly consistent with the calculated DOS results (Figure 1). The remarkably increased N_D would help to enhance the charge transport in the Co-doped In_2S_3 3ALs and at the interface with ITO substrate, which is further demonstrated by their corresponding electrochemical impedance spectra (Figure 4D).[2–4] Accordingly, our synthesized Co doping confined in In_2S_3 3ALs can fully optimize the elementary visible-light absorption, separation of photoexcited hole–electron pairs, and transfer of photoexcited electrons through the external circuit, thus achieving superior visible-light water splitting.

In conclusion, a conceptually new model of doping confined in atomic layers is proposed as an exotic platform for gaining atomic-level insights into the role of elemental doping in photocatalysis. As a proof-of-concept prototype, Co doping confined in three atomic layers of In_2S_3 are first successfully synthesized through a scalable lamellar inorganic–organic hybrid intermediate strategy. DFT calculations disclose that the splitting of Co 3d states brings the In_2S_3 atomic layers with several new energy levels, in which the photogenerated electrons can be easily excited by the d→d internal transitions of Co ions under solar light irradiation, as verified by the sharply increased values in the UV/Vis absorption and IPCE measurements. Moreover, ultrafast transient absorption spectroscopy reveals that the Co doping results in ultrashort photogenerated electron transfer time of about 1.6 ps from the valence band of In_2S_3 to the newly formed localized states, while the circa 25-fold increase in average recovery lifetime suggests remarkably promoted electron-hole separation efficacy. Furthermore, the calculated DOS illustrates that the Co doping leads to a higher DOS near the CBM, beneficial for three times higher carrier concentration as revealed by the Mott–Schottky curve. Thanks to the above advantages, the Co-doped In_2S_3 three atomic layers reach a photocurrent density up to 1.17 $mA\,cm^{-2}$ at 1.5 V (vs. RHE), nearly 10 and 17 times larger than that of the perfect In_2S_3 (three atomic layers) and bulk counterpart, respectively. This work provides a facile and convenient strategy for fabricating cation doping confined in atomic layers and hence gains crucial atomic-level insights into the role of elemental doping in photocatalysis through deeply studying the involved three elementary processes, thus opening up new possibilities for manipulating solar water splitting properties.

Keywords: atomic layers · cobalt · doping · ultrafast transient absorption spectroscopy · water splitting

How to cite: *Angew. Chem. Int. Ed.* **2015**, *54*, 9266–9270
Angew. Chem. **2015**, *127*, 9398–9402

[1] X. B. Chen, L. Liu, P. Y. Yu, S. S. Mao, *Science* **2011**, *331*, 746–750.
[2] Y. F. Sun, Z. H. Sun, S. Gao, H. Cheng, Q. H. Liu, J. Y. Piao, T. Yao, C. Z. Wu, S. L. Hu, S. Q. Wei, Y. Xie, *Nat. Commun.* **2012**, *3*, 1057.
[3] Y. F. Sun, H. Cheng, S. Gao, Z. H. Sun, Q. H. Liu, Q. Liu, F. C. Lei, T. Yao, J. F. He, S. Q. Wei, Y. Xie, *Angew. Chem. Int. Ed.* **2012**, *51*, 8727–8731; *Angew. Chem.* **2012**, *124*, 8857–8861.
[4] F. C. Lei, Y. F. Sun, K. T. Liu, S. Gao, L. Liang, B. C. Pan, Y. Xie, *J. Am. Chem. Soc.* **2014**, *136*, 6826–6829.
[5] W. N. Wang, W. J. An, B. Ramalingam, S. Mukherjee, D. M. Niedzwiedzki, S. Gangopadhyay, P. Biswas, *J. Am. Chem. Soc.* **2012**, *134*, 11276–11281.
[6] G. Wang, H. Wang, Y. Ling, Y. Tang, X. Yang, R. C. Fitzmorris, C. Wang, J. Z. Zhang, Y. Li, *Nano Lett.* **2011**, *11*, 3026–3033.
[7] T. W. Kim, K. S. Choi, *Science* **2014**, *343*, 990.
[8] J. S. Luo, J. H. Im, M. T. Mayer, M. Schreier, M. K. Nazeeruddin, N. G. Park, S. D. Tilley, H. J. Fan, M. Grätzel, *Science* **2014**, *345*, 1593.
[9] F. F. Abdi, L. H. Han, A. H. M. Smets, M. Zeman, B. Dam, R. V. D. Krol, *Nat. Commun.* **2013**, *4*, 2195.
[10] Y. F. Sun, Z. H. Sun, S. Gao, H. Cheng, Q. H. Liu, F. C. Lei, S. Q. Wei, Y. Xie, *Adv. Energy Mater.* **2014**, *4*, 1300611.
[11] Y. F. Sun, S. Gao, Y. Xie, *Chem. Soc. Rev.* **2014**, *43*, 530–546.
[12] Y. H. Peng, G. F. Huang, W. Q. Huang, *Adv. Powder Technol.* **2012**, *23*, 8–12.
[13] S. Li, P. Jena, *Phys. Rev. B* **2009**, *79*, 201204.
[14] S. Kuriakose, B. Satpati, S. Mohapatra, *Phys. Chem. Chem. Phys.* **2014**, *16*, 12741–12749.
[15] X. Chen, S. S. Mao, *Chem. Rev.* **2007**, *107*, 2891–2959.
[16] C. Z. Wang, Z. Chen, H. B. Jin, C. B. Cao, J. B. Li, Z. T. Mi, *J. Mater. Chem. A* **2014**, *2*, 17820–17827.
[17] Y. J. Hsiao, C. H. Lu, L. W. Ji, T. H. Meen, Y. L. Chen, H. P. Chi, *Nanoscale Res. Lett.* **2014**, *9*, 32.
[18] A. Walsh, J. L. F. Da Silva, S.-H. Wei, *Phys. Rev. Lett.* **2008**, *100*, 256401.
[19] Y. C. Lu, Y. H. Lin, D. J. Wang, L. L. Wang, T. F. Xie, T. F. Jiang, *Nano Res.* **2011**, *4*, 1144–1152.
[20] Y. F. Sun, Q. H. Liu, S. Gao, H. Cheng, F. C. Lei, Z. H. Sun, Y. Jiang, H. B. Su, S. Q. Wei, Y. Xie, *Nat. Commun.* **2013**, *4*, 2899.
[21] S. Gao, Y. F. Sun, F. C. Lei, J. W. Liu, L. Liang, T. W. Li, B. C. Pan, J. F. Zhou, Y. Xie, *Nano Energy* **2014**, *3*, 205–213.
[22] Y. F. Sun, H. Cheng, S. Gao, Q. H. Liu, Z. H. Sun, C. Xiao, C. Z. Wu, S. P. Wei, Y. Xie, *J. Am. Chem. Soc.* **2012**, *134*, 20294–20297.
[23] Y. F. Sun, Y. Xie, C. Z. Wu, S. D. Zhang, S. S. Jiang, *Nano Res.* **2010**, *3*, 620–631.
[24] L. Liang, Y. F. Sun, F. C. Lei, S. Gao, Y. Xie, *J. Mater. Chem. A* **2014**, *2*, 10647–10653.
[25] M. Ueno, H. Nakanishi, T. Irie, *J. Phys. Soc. Jpn.* **1978**, *44*, 2013–2014.

Received: April 15, 2015
Revised: May 23, 2015
Published online: June 25, 2015

